TU Delft

Delft University of Technology

Oxidation fronts and oxide scale growth modeling in spark plasma sintered ZrC ultra-high temperature ceramic

Lin, Yun Ching; Huizenga, Richard; Kim, Hyun Sik; Brouwer, Hans; Armaki, Amir Mohseni; Popovich, Vera; Tang, Yinglu

DOI
10.1016/j.jeurceramsoc.2025.117976

Licence
CC BY

Publication date
2026

Document Version
Final published version

Published in
Journal of the European Ceramic Society

Citation (APA)
Lin, Y. C., Huizenga, R., Kim, H. S., Brouwer, H., Armaki, A. M., Popovich, V., & Tang, Y. (2026). Oxidation fronts and oxide scale growth modeling in spark plasma sintered ZrC ultra-high temperature ceramic. *Journal of the European Ceramic Society*, *46*(4), Article 117976. https://doi.org/10.1016/j.jeurceramsoc.2025.117976

Important note
To cite this publication, please use the final published version (if applicable).
Please check the document version above.

Copyright
Other than for strictly personal use, it is not permitted to download, forward or distribute the text or part of it, without the consent of the author(s) and/or copyright holder(s), unless the work is under an open content license such as Creative Commons.

Takedown policy
Please contact us and provide details if you believe this document breaches copyrights.
We will remove access to the work immediately and investigate your claim.

This work is downloaded from Delft University of Technology.
For technical reasons the number of authors shown on this cover page is limited to a maximum of 10.

Journal of the European Ceramic Society 46 (2026) 117976

Contents lists available at ScienceDirect

Journal of the European Ceramic Society

journal homepage: www.elsevier.com/locate/jeurceramsoc

Oxidation fronts and oxide scale growth modeling in spark plasma sintered ZrC ultra-high temperature ceramic

Yun-Ching Lin [a,*], Richard Huizenga [b], Hyun-Sik Kim [c], Hans Brouwer [b], Amir Mohseni Armaki [b], Vera Popovich [b], Yinglu Tang [a,*]

[a] Department of Aerospace Structures and Materials, Faculty of Aerospace Engineering, Delft University of Technology, Kluyverweg 1, Delft 2629 HS, The Netherlands
[b] Department of Materials Science and Engineering, Faculty of Mechanical Engineering, Delft University of Technology, Mekelweg 2, Delft 2628 CD, The Netherlands
[c] Department of Materials Science and Engineering, University of Seoul, Seoul 02504, Republic of Korea

ARTICLE INFO

Keywords:
Zirconium carbide (ZrC)
Zr–C–O layer
Oxidation front stripe
Elliptical submicropore
Oxide scale growth model

ABSTRACT

Zirconium carbide (ZrC) is a candidate material for extreme environments due to its exceptional thermal and mechanical properties. However, its oxidation behavior, particularly the formation of the Zr–C–O layer, requires further clarification. In this study, we investigated the oxidation of spark plasma sintered ZrC under varying temperatures and oxygen partial pressures, revealing a double-layer oxide scale. At the interface between ZrC and the Zr–C–O layer, we identified previously unreported oxidation front stripes composed of cubic zirconia, along which elliptical submicropores formed, suggesting preferential CO_2 release pathways. The Zr–C–O layer itself was significantly enriched with amorphous free carbon. Based on these findings, we developed a phenomenological model that incorporated the formation of the compact Zr–C–O layer to predict oxide scale growth. This multiscale approach provides new insights into ZrC oxidation mechanisms and supports the design of oxidation-resistant ceramics for aerospace and nuclear applications.

1. Introduction

Materials for extreme environments, such as those encountered in aerospace and nuclear systems [1–4], must withstand high temperatures and oxidative conditions. Zirconium carbide (ZrC), with its high hardness (25 GPa) [1], excellent wear resistance [2], and high congruent melting point above 3500 °C [5], is a promising candidate. However, its poor oxidation resistance above 500 °C limits its practical applications. The oxidation behavior of ZrC [6,7] was investigated in previous studies, and a Zr–C–O layer [8–12] was reported which remained compact serving as a potential barrier layer [8,13,14] to mitigate high-temperature oxidation. Although the compact Zr–C–O layer has been observed, its formation mechanism and composition at the oxidation front require further elucidation. Divergent interpretations of the Zr–C–O layer and ZrC oxidation mechanisms have emerged in the literature [9,11,15–17] due to the complexity of the heterogeneous oxidation reactions and the difficulty in distinguishing between ZrC and zirconium oxycarbide (ZrC_xO_y), both of which exhibit a face-centered cubic (FCC) structure with negligible differences in their lattice parameters [11,16].

Although a ZrC_xO_y layer has not yet been directly observed experimentally by most researchers, its formation is frequently postulated due to the substitutional solubility of oxygen in ZrC. It is considered a plausible intermediate during the early stages of ZrC oxidation and as a representation of the Zr–C–O layer [15,16,18].

Bartlett et al. [15] studied ZrC powder at 450−580 °C and in oxygen partial pressures of 6.5×10^{-3}–100 % O_2. They reported the transport of atomic oxygen into the ZrC lattice, replacing carbon and forming ZrC_xO_y, with the diffusion process supported by kinetic calculations based on weight gain measurements. The observed weight gain for the diffusion process corresponded to 12 % of the total increase associated with the full oxidation of ZrC to ZrO_2. This value matched the weight increase expected from a 60 % replacement of carbon by oxygen in ZrC. However, no microscopic observations or supporting analyses were provided to substantiate this explanation. Besides, the solubility of oxygen in ZrC at the investigated temperature range remains unclear, particularly with respect to its potential to reach 60 % oxygen substitution for carbon.

Rao et al. [16] also studied ZrC powder, under the temperature range 277–1027 °C and oxygen partial pressures of 5−50 % O_2. They proposed

* Corresponding authors.
E-mail addresses: Y.Lin-4@tudelft.nl (Y.-C. Lin), Y.Tang-5@tudelft.nl (Y. Tang).

https://doi.org/10.1016/j.jeurceramsoc.2025.117976
Received 19 September 2025; Received in revised form 28 October 2025; Accepted 10 November 2025
Available online 11 November 2025
0955-2219/© 2025 The Author(s). Published by Elsevier Ltd. This is an open access article under the CC BY license (http://creativecommons.org/licenses/by/4.0/).

a model which involved oxygen diffusion through the matrix with the formation of oxycarbide and free carbon associated with the stabilization of cubic ZrO_2 (c-ZrO_2). The competing mechanisms involved can be summarized into the following three reactions:

$$ZrC + \frac{1}{2}(1-x)O_{2(g)} \rightarrow ZrC_xO_{1-x} + (1-x)C \quad (1)$$

$$ZrC_xO_{1-x} + \frac{1}{2}(1+3x)O_{2(g)} \rightarrow ZrO_2 + xCO_{2(g)} \quad (2)$$

$$C + O_{2(g)} \rightarrow CO_{2(g)} \quad (3)$$

Eq. (1) indicates that zirconium oxycarbide and carbon are initally formed at the reaction front and interfacial region. Subsequently, zirconium oxycarbide transforms into ZrO_2 and gaeous CO_2. Moerover, carbon generated in Eq. (1) independently oxidizes to form CO_2 (Eq. (3)), separate from the zirconia formation process (Eq. (2)).

Shimada et al. in 1990 [18] studied powdered ZrC oxidized under temperature range 380−550 °C and oxygen partial pressure range 1.3−7.9 % O_2. They reported the rapid formation of ZrC_xO_y in the early-stage oxidation within 5−10 min, followed by nucleation of c-ZrO_2 from oxycarbide, which they concluded based on the weight gain of ZrC upon oxidation. However, in 1995, they studied ZrC single crystals and proposed that the oxide scale consisted of two subscales, namely zone 1 and zone 2 [17]. Zone 1 was a pore-free layer composed of amorphous ZrO_{2-x} phase, some c-ZrO_2 particles, and rich carbon. Meanwhile, zone 2 was a cracked layer consisting of aggregated c-ZrO_2 with carbon depletion. In 1996 [10] and 1997 [19], they again proposed oxycarbide $ZrC_{1-x}O_x$ ($x < 0.4$) formation by using the results of relative count ratios of C and O to Zr across the interface determined by EDX with ZrC single crystals. In 1998, they studied ZrC single crystals and reported, based on TEM results, that zone 1 film was composed of regular lattice fringes corresponding to c-ZrO_2 and an amorphous carbon phase [20]. Tetragonal ZrO_2 (t-ZrO_2) and monoclinic ZrO_2 (m-ZrO_2) particles also occurred in the film [21]. Ultimately, in 2001 [22,23], they proposed interfacial reactions on oxidation of carbides based on studies with carbide single crystals. As the culmination of their investigations, they suggested the following interfacial reactions between the carbide and zone 1, as well as between zones 1 and 2.

(1) Early-stage carbide/O_2 interface

Formation of oxycarbide and CO_2:

$$MeC + \frac{3x}{2}O_2 \rightarrow MeC_{1-x}O_x + xCO_2 \ (\mathrm{Me} = \mathrm{Zr, Hf, Ti}) \quad (4)$$

(2) Carbide/zone 1 interface

Oxycarbide was saturated with oxygen at $x \approx 0.4$ producing MeO_2 and carbon:

$$MeC_{1-x}O_x + \frac{1-x}{2}O_2 \rightarrow MeO_2 + (1-x)C \quad (5)$$

(3) Zone 1/2 interface

Zone 2 was cracked and therefore O_2 gas can easily penetrate to the front of zone 1 where the remaining carbon was oxidized into CO_2:

$$C(zone\ 1) + O_2 \rightarrow CO_2 \quad (6)$$

Gasparrini et al. [9] reported that the Zr–C–O layer should comprise zirconia along with free carbon rather than ZrC_xO_y by investigating hot-pressed ZrC oxidized at 800 °C in 21 % O_2 for 3600 s. The oxidation temperature domain extended into higher regimes compared to that of Bartlett [15] and Shimada [19–22]. They identified a 2 μm thick Zr–C–O layer composed of an amorphous carbon matrix with ZrO_2 nanocrystals embedded in the matrix between ZrC and ZrO_2, which offered experimental corroboration of the products described in Eq. (5). However, the oxycarbide in Eq. (4) was not identified.

Bellucci et al. [11] reported c-ZrO_2 and m-ZrO_2 with retained carbon with ZrC single crystals oxidized at around 700 °C in Ar/O_2 mixtures at three O_2 composition: 1.06×10^{-2}, 1.19×10^{-2}, and 1.31×10^{-2} % O_2. They identified amorphous carbon retained in the sample via AES analysis and the presence of both the c-ZrO_2 and m-ZrO_2 by XRD and Raman analysis; nevertheless, oxycarbide was not observed.

Kwon et al. [24] explored the interaction between oxygen and metal carbide surfaces during early oxidation by combining density functional theory (DFT), ab initio molecular dynamics (AIMD), and metadynamics (MTD) simulations. Through the multifaceted approach, they examined oxygen adsorption, reaction, CO formation, and diffusion behaviors on ZrC (100) surface. The results demonstrated the formation of zirconium oxycarbide in early-stage oxidation, which involved strong O adsorption, followed by CO formation and O diffusion into vacant carbon sites.

The key observations and interpretations reported in previous studies are summarized in Table 1. The literature reveals inconsistencies and contradictions concerning the Zr–C–O layer and oxidation mechanisms. To clarify the mechanistic role and existence of oxycarbide during oxidation, we conducted static oxidation experiments on near-stoichiometric spark plasma sintered ZrC over the temperature range of 600–1000 °C and oxygen partial pressures of 2.0–21.0 % O_2, followed by detailed characterization of the various oxidized regions and interfaces.

Beyond microscopic-scale investigations, several oxidation models were proposed to capture the oxidation behavior of ZrC at mesoscopic and macroscopic scales by using linear rate law or Jander's equation [18]. Hou et al. [25] further investigated the effects of temperature and oxygen partial pressure on ZrC oxidation kinetics using the Chou's model [26,27]. They reported that the Chou's model [26,27] performed accurate prediction of the oxidation kinetics of ZrC in comparison with the previous linear and Jander's models from a quantitative standpoint based on the experimental data offered by Shimada et al. [18] and Kuriakose et al. [28]. A key factor which distinguished the Chou's model from others was its capacity to capture the relationship between the reacted fraction, temperature, and oxygen partial pressure.

Although previous models have considered the coupled effects of temperature and oxygen partial pressure, a critical aspect with respect to the different oxidation stages of ZrC has been largely neglected in prior research. Lin et al. [29] reported a k_1 parabolic oxidation regime during ZrC oxidation, during which solely a compact Zr–C–O monolayer formed without through-thickness cracks due to limited CO_2 formation (Eq. (6)). The parabolic regime was governed by a duration in which a diffusion-limiting dense oxide scale remained stable before significant through-thickness cracking, which initiated the transition to the k_3 linear regime. Therefore, we developed the first phenomenological model to describe the oxide scale thickness growth in spark plasma sintered ZrC, featuring the compact Zr–C–O layer formation—a mechanistic aspect not systematically addressed in prior established models. The model encompassed the dynamic evolution of outer-layer oxide scale thickness across mesoscopic and macroscopic regimes under 600–800 °C and 2.0–21.0 % O_2.

This study aims to provide a comprehensive investigation of oxide growth in ZrC across all relevant length scales, ranging from nanoscale and microscopic-level analysis via HRTEM to mesoscopic and macroscopic scales, complemented by the development of a robust phenomenological model which is capable of capturing the oxide scale thickness evolution.

2. Materials and methods

2.1. Material fabrication

Zirconium carbide (ZrC) powder (purity: 99.5 %, particle size < 45 μm, Goodfellow, UK) was used as the sole starting material. The

Table 1
Summary of key studies on ZrC oxidation, highlighting experimental conditions, observed oxide scale structures, and interpretations of oxycarbide formation.

Study	ZrC form	Temp (°C)	PO_2 (% O_2)	Key observations	Proposed oxidation products / layers	Techniques / notes
Bartlett et al. [15]	Powder	450–580	6.5×10^{-3}–100	Atomic O diffusion into lattice replacing C; ~12 % weight gain (60 % C substitution)	Oxycarbide; O dissolution in ZrC lattice	Kinetic modeling based on weight gain; no microstructural confirmation
Rao et al. [16]	Powder	277–1027	5–50	O diffusion through matrix; free C formation	Oxycarbide + C; stabilization of c-ZrO_2	Conceptual oxidation model
Shimada et al. (1990–2001) 1990 [18] 1995 [17] 1996 [10] 1997 [19] 1998 [20,21] 2001 [22,23]	Powder and single crystals	380–550	1.3–7.9	Early oxycarbide formation (5–10 min); two-zone oxide scale structure	Zone 1 (amorphous ZrO_{2-x} + C) and Zone 2 (c-ZrO_2); later studies showed amorphous C films and t/m-ZrO_2 nanocrystals	Weight gain kinetics, EDX, and TEM; progressive model of oxycarbide formation and crystallization
Gasparrini et al. [9]	Hot-pressed	800	21	2 μm Zr–C–O layer between ZrC and ZrO_2	Amorphous C matrix + ZrO_2 nanocrystals; no oxycarbide	TEM and phase contrast
Bellucci et al. [11]	Single crystals	~700	1.06×10^{-2}–1.31×10^{-2}	Retained amorphous C; c-ZrO_2 and m-ZrO_2 detected	ZrO_2 + residual C; no oxycarbide	AES, XRD, and Raman
Kwon et al. [24]	(100) surface (DFT/ AIMD/ MTD)	— (Simulation)	—	Early-stage oxidation: O adsorption → CO formation → O diffusion	Oxycarbide formation during initial oxidation	First-principles and metadynamics simulations

powder was placed into a 30 mm diameter graphite die inside a glovebox to minimize oxygen contamination, then transferred to a spark plasma sintering (SPS) furnace (FCT Systeme GmbH, Germany) and sintered under vacuum. A two-step sintering process was carried out: 1500 °C for 120 s followed by 2000 °C for 600 s under 80 MPa uniaxial pressure, with a heating rate of 3.3 °C/s. The initial 1500 °C hold was intended to minimize contamination prior to high-temperature sintering. After sintering, the sample was cooled to room temperature with a cooling rate of 0.4 °C/s and surface graphite was removed using a grinder-polisher (MetaServ 250, Buehler, USA). The resulting ZrC disk had a relative density of 98.7 ± 0.1 % calculated by the Archimedes method. The ZrC disk was polished with progressively finer grit papers, culminating in a mirror-like surface using a 1 μm polishing cloth. Lastly, the ceramic disk was machined into rectangular cuboids with dimensions 6 × 6 × 3 mm^3 using a precision cutting machine (Secotom-60, Struers, Denmark) equipped with a diamond cut-off wheel (M1D20). A total of 24 ZrC cuboids of the same dimensions were prepared for subsequent isothermal static oxidation tests.

2.2. Isothermal static oxidation

Static oxidation was carried out by the ZrC rectangular cuboids placed on a crucible in TGA furnace (Seteram TAG 16/18, France) heated with 0.08 °C/s in a flow of pure argon. When the target temperature was reached, oxygen was then added to the argon gas flow with controlled oxygen partial pressure during the isothermal hold. Isothermal oxidation tests were conducted at temperatures of 600–1000 °C under oxygen partial pressures of 2.0–21.0 % O_2 for isothermal oxidation durations ranging from 1500 s up to 32400 s. Stable conditions during the isothermal hold were ensured by admitting the oxygen–argon gas mixture through mass flow controllers (Bronkhorst, Netherlands), and real-time monitoring of oxygen partial pressure and temperature with LabVIEW (version 2020) and Pt/Pt–10 %Rh (S-type) thermocouples. Prior to introducing gas mixture into the furnace, oxygen and argon were filtered to remove residual moisture and hydrocarbons with Hydrosorb (< 20 ppb H_2O) and Accosorb (< 10 ppb hydrocarbons) filters (Messer Griesheim, Germany) respectively. Argon was additionally filtered to remove residual oxygen with an Oxysorb filter (< 5 ppb O_2). Following the isothermal hold, the TGA furnace was cooled to ambient temperature at a rate of 0.08 °C/s under pure argon.

2.3. Characterization

The microstructures of the surfaces and cross-sections of oxidized SPS-sintered ZrC were analyzed by scanning electron microscopy (SEM) using a JSM-IT 100 (JEOL, Japan). The Zr–C–O layer and oxidation front stripes were investigated via high-resolution transmission electron microscopy (HRTEM) using a double Cs-corrected JEM-ARM200F apparatus (JEOL, Japan) and energy-dispersive X-ray spectroscopy (EDX) carried out with a Dual SDD EDS system (JEOL, Japan).

The lamella for HRTEM was prepared with focused ion beam (FIB) (Helios G5 UC, Thermo Fisher Scientific, USA) with a Ga-focused ion beam. A protective platinum layer approximately 2–3 μm thick was first deposited on the region of interest via electron- and ion-assisted deposition. Regions for FIB sectioning were selected based on SEM imaging of representative oxidation features. Coarse milling was performed using a 30 kV Ga^+ ion beam at high current (2.5–21 nA) to excavate trenches on either side of the lamella. The sample was then thinned to electron transparency using progressively lower ion beam currents (0.43 nA–1.1 pA). The lamella was lifted out using an in-situ NanoManipulator (EasyLift system) and mounted onto a copper half-grid using ion-assisted Pt deposition.

The outer-layer scale was characterized via X-ray diffractometry (XRD) and Raman spectroscopy. XRD analysis was carried out using a D8 Advance diffractometer (Bruker, Germany) configured in Bragg–Brentano geometry and equipped with a LynxEye position-sensitive

detector, operated with Cu Kα radiation. Diffractograms were recorded in the 2θ range of 10–100° with a 2θ step size of 0.033° and a counting time per step of 2 s. Data were analyzed via Bruker software DiffracSuite.EVA vs 7.1.

Raman spectroscopy was performed in backscattering geometry using a Raman imaging microscope (Alpha300 R, WITec, Germany) with a 532 nm excitation laser. A 50× Zeiss objective (working distance 9.1 mm) was used to focus the beam on the sample surface. The laser power at the sample was set to 25 mW, which provided sufficient signal intensity while avoiding noticeable laser-induced heating or surface modification. Each spectrum was acquired with an integration time of 8 s and averaged over 10 accumulations to enhance the signal-to-noise ratio. A grating with 1800 lines/mm was employed, yielding a spectral resolution better than 1 cm^{-1} and allowing clear separation of closely spaced vibrational modes. The spectrometer was calibrated using an argon–mercury lamp prior to measurements to ensure spectral accuracy.

3. Results and discussion

3.1. Double-layer oxide scale and oxidation front stripe

3.1.1. Morphologies of oxidized layers, oxidation fronts, and submicropores

The double-layer oxide scale (inner layer + outer layer) and the oxidation front stripes were observed for ZrC oxidized under temperatures 600–700 °C and oxygen partial pressures 2–21 % O_2. The definitions of the terminology used to describe the distinct regions of the oxidized ZrC based on combined HRTEM, XRD and Raman data are provided in Table 2, and their corresponding locations are depicted in Fig. 1(a)(b).

The double-layer oxide scale was composed of a compact Zr–C–O layer and a cracked outer layer. The oxidation front stripes were located at the interface of ZrC and Zr–C–O layer. The SEM image of the lamella of ZrC oxidized under 600 °C and 2 % O_2 for 10800 s, as shown in Fig. 1 (a), depicts the double-layer oxide scale. The scanning transmission electron microscopy (STEM) image of the lamella at the ZrC substrate/Zr–C–O layer interface (Fig. 1(b)) shows the morphology of oxidation front stripes. STEM revealed that the oxidation front stripe possessed a width of 86 ± 50 nm.

Accommodated along these oxidation front stripes, high-aspect-ratio elliptical submicropores were revealed via STEM, characterized by a major axis of 217 ± 83 nm and a minor axis of 35 ± 13 nm, as shown in Fig. 1(b). These elliptical submicropores suggested the locations of CO_2 bubble formation in early-stage oxidation, which indicated the preferential pathways for CO_2 release. The minor axes of the submicropores were compressed perpendicular to nominal pristine ZrC surface, which indicated localized anisotropic stress and pressure buildup occurring during CO_2 evolution under oxidative conditions. The rapid CO_2 formation and accumulation along the oxidation front stripes at elevated oxygen partial pressures induced localized pressurization perpendicular to the nominal pristine ZrC surface, preferentially driving lateral expansion of the pores and resulting in elongated pores with a high average aspect ratio (major axis/minor axis) ≈ 6.2.

The confinement of CO_2 bubbles compressed along the oxidation front stripes may reflect kinetic limitations on CO_2 gas escape and directional mechanical constraints imposed by the oxidation environment. While the observed pore morphology suggests directional stress and gas confinement, further in-situ studies are needed to confirm this mechanism.

3.1.2. Composition of oxidation front stripes, oxidized layers, and interfaces

HRTEM was employed to investigate the composition and crystal structure of the oxidation front stripes, oxidized layers, and interfacial regions. Fig. 2(a) displays a TEM micrograph at the ZrC/Zr–C–O layer interface, marking the regions selected for HRTEM analysis. By fast fourier transform (FFT) of the location outside and within the oxidation front stripe (shown in Square III and Square IV in Fig. 3(a) respectively), we identified the composition of the oxidation front stripe to be c-ZrO_2 (Fig. 3(c)), which showed a similar cubic diffraction pattern as the selected area electron diffraction pattern (SAEDP) of outer-layer oxide scale formed under oxidation conditions: 600 °C, 2 % O_2, 10800 s (Fig. 1 (f)). Furthermore, HRTEM-EDX line analysis showed a saturation of O at % at the oxidation front stripe (Fig. 2(b)) with a O/Zr at% ratio ≈ 2, which also supported the formation of stoichiometric ZrO_2. This is coherent with the results from FFT which demonstrated the existence of c-ZrO_2 in the oxidation front stripe.

First-principles studies indicate that c-ZrO_2 preferentially nucleates on ZrC along specific crystallographic orientations, such as the (100) [30–32] and (111) [33,34] surfaces. Preferred-orientation growth of c-ZrO_2 on these surfaces could induce interfacial stress, promoting the formation of the observed stripe-like morphology. Other factors, including microstructural defects and kinetic limitations, may further enhance branching and the development of these stripe patterns. Apart from the c-ZrO_2 phase, there was appearance of a subtle halo ring which suggested the formation of amorphous free carbon in the oxidation front stripe. The region outside the oxidation front stripe showed the pattern of ZrC (Fig. 3(b)), which exhibited a similar diffraction pattern as the SAEDP of the ZrC substrate (Fig. 1(d)).

The outer-layer oxide scale and Zr–C–O layer were also characterized via HRTEM. HRTEM images and SAEDP confirmed the presence of ZrC in the substrate (Fig. 1(c)(d)) and c-ZrO_2 in the outer-layer oxide scale (Fig. 1(e)(f)). The HRTEM image of the Zr–C–O layer (right-hand side of Fig. 3(d)), along with its corresponding FFT pattern (Fig. 3(f)), revealed a diffuse ring corresponding to an average interatomic spacing of approximately 3.4 Å, rather than distinct diffraction spots. The broad and diffuse ring corresponded to an average interatomic spacing of approximately 3.4 Å, which was indicative of the short-range order typical of amorphous carbon. The Zr–C–O layer exhibited a substantial presence of amorphous free carbon, which overlapped and obscured the diffraction spots corresponding to ZrO_2 (Fig. 3(f)). Although the strong amorphous carbon halo partially overlapped with the ZrO_2 diffraction spots, the FFT diffraction patterns obtained from the oxidation front

Table 2
Definitions of terminology for the distinct regions of oxidized ZrC based on combined HRTEM, XRD, and Raman data.

Terminology	Definition
Double-layer oxide scale	A non-uniform oxide scale structure formed on ZrC during oxidation, characterized by two morphologically distinct layers with significantly disparate carbon contents: an inner layer and an outer layer
Inner layer (Zr–C–O layer)	A structurally dense layer exhibiting significant enrichment of amorphous carbon content adherent to the ZrC substrate
Outer layer	A structurally cracked and porous layer with minimal amorphous carbon content, physically connected to the inner layer but not in direct contact with the ZrC substrate
Oxidation front stripe	A microstructural stripe pattern located at the ZrC substrate/Zr–C–O layer interface and in the Zr–C–O layer, characterized by dendritic feature extending into the ZrC substrate

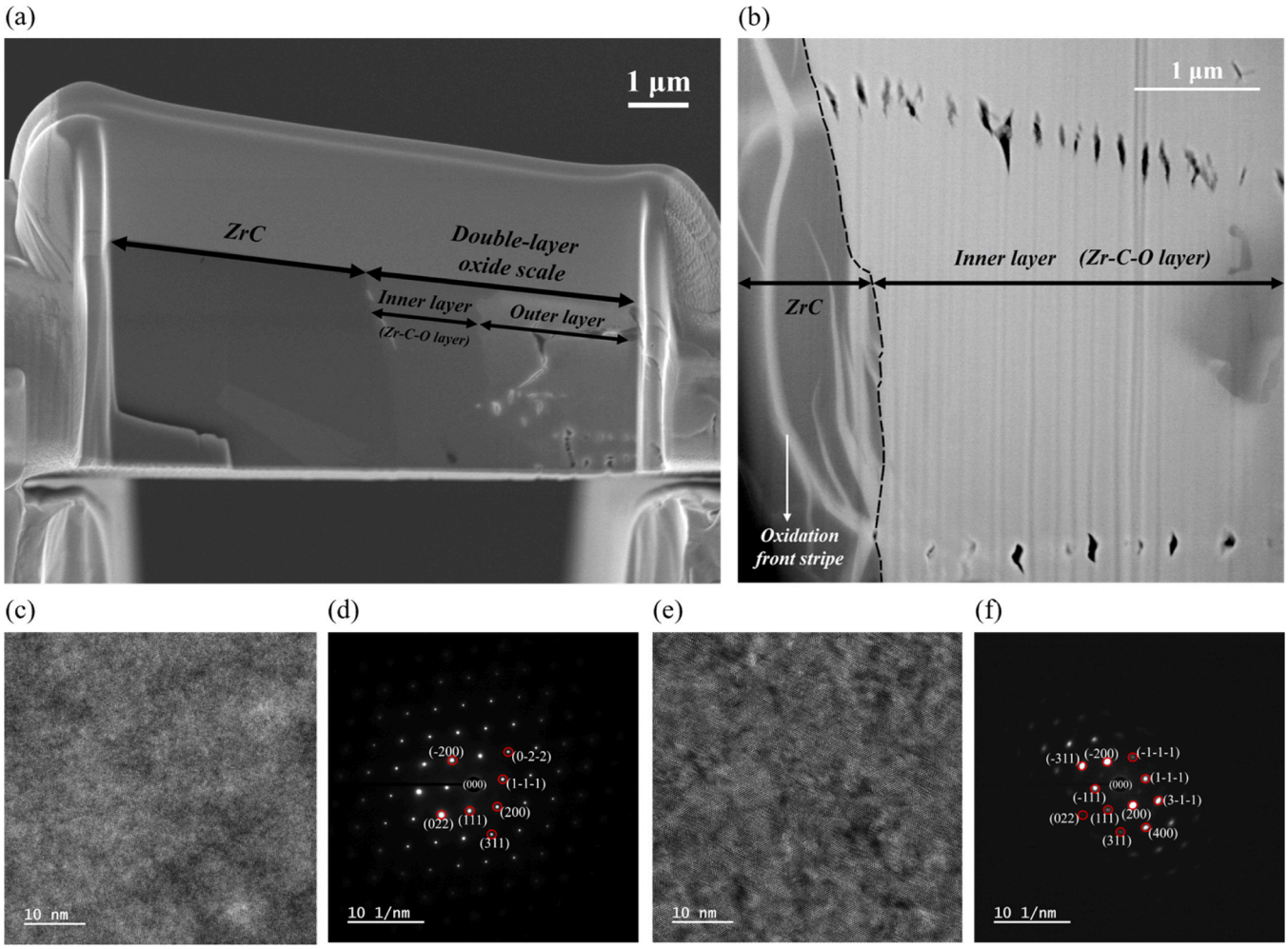

Fig. 1. (a) SEM image of the oxidized ZrC lamella (oxidation conditions: 600 °C; 2 % O_2; 10800 s). The double-layer oxide scale on ZrC substrate is demonstrated in the image. (b) STEM image HAADF mode of the oxidized ZrC lamella (600 °C; 2 % O_2; 10800 s) at the ZrC substrate/Zr–C–O layer interface, revealing the compact Zr–C–O layer, the oxidation front stripes, and the submicropores along the oxidation front stripe patterns. The black dashed line is the interface of ZrC substrate and Zr–C–O layer. (c) HRTEM image of ZrC substrate of the lamella in (a). (d) Selected area electron diffraction pattern (SAEDP) of ZrC substrate of the lamella in (a) with zone axis: [01−1]. The interplanar spacings (d_{hkl}) are approximately: 2.72 Å for d_{111}, 2.36 Å for d_{200}, 1.66 Å for d_{220}, and 1.42 Å for d_{311}, which are consistent with the face-centered cubic crystal structure of ZrC. (e) HRTEM image of outer-layer oxide scale of the lamella in (a). (f) SAEDP of outer-layer oxide scale of the lamella in (a) with zone axis: [01−1]. The interplanar spacings (d_{hkl}) are approximately: 2.94 Å for d_{111}, 2.55 Å for d_{200}, 1.80 Å for d_{220}, 1.54 Å for d_{311}, and 1.27 Å for d_{400}, which are consistent with the cubic crystal structure of ZrO_2 (c-ZrO_2).

stripes (Fig. 3(c)) clearly exhibited c-ZrO_2 formation. Similarly, the SAEDP of the outer-layer oxide scale (Fig. 1(f)) confirmed the presence of c-ZrO_2. Given that the Zr–C–O layer is located between the oxidation front stripes and the outer-layer oxide scale, both of which consist of c-ZrO_2, and is positioned farther from the oxidation front (Fig. 4) than the oxidation stripes, these observations support that the Zr–C–O layer also contains ZrO_2. Moreover, HRTEM-EDX analysis revealed that the oxygen concentration in the Zr–C–O layer reached a saturation level (Fig. 2(c)). This saturation behavior indicates that this layer is fully oxidized, consistent with the formation of zirconia rather than an oxycarbide phase. Collectively, these results confirm that the Zr–C–O layer consists of zirconia coexisting with a substantial amount of amorphous free carbon.

Based on comprehensive analyses using HRTEM, SAED, FFT, and HRTEM-EDX, we confirm that neither the oxidation front stripes nor the Zr–C–O layer corresponds to a zirconium oxycarbide phase. Instead, both are composed of c-ZrO_2 embedded in an amorphous carbon matrix, with a pronounced enrichment of amorphous free carbon in the Zr–C–O layer.

Although oxycarbide was not identified in the oxidation front stripe and Zr–C–O layer, HRTEM-EDX line scans revealed the regions where O at% started to incline, but prior to reaching its saturation (depicted by purple dashed squares in Fig. 2(b)(c)), the O to Zr at% ratio remained below 2. These nanometer-scale regions, specifically a 10 nm proximal zone contiguous with the oxidation front stripe and a 20−30 nm proximal zone adjacent to the Zr–C–O layer, featured a low O at%. Such localized regions could correspond to an oxycarbide, and may be revealed by HRTEM-EDX profiles. This experimental observation aligns with the findings reported by Kwon et al. [24] through combined DFT, AIMD, and MTD simulations. Their calculation suggested that the early stages of oxidation at the ZrC surface involved strong oxygen adsorption, followed by O diffusion into vacant carbon sites, ultimately leading to zirconium oxycarbide formation.

3.2. Composition and phase evolution of outer-layer oxide scale

3.2.1. Zirconia phase evolution and carbon retention

Outer-layer oxide scales formed at temperatures 600–1000 °C under 2 % O_2 with oxidation durations up to 32400 s were analyzed via XRD and Raman spectroscopy. At 600 °C, XRD revealed primarily c-ZrO_2 with peak broadening (Fig. 5(a)(b)), which suggested nanocrystalline domains [19]. Due to this broadening, the presence of t-ZrO_2 could not be

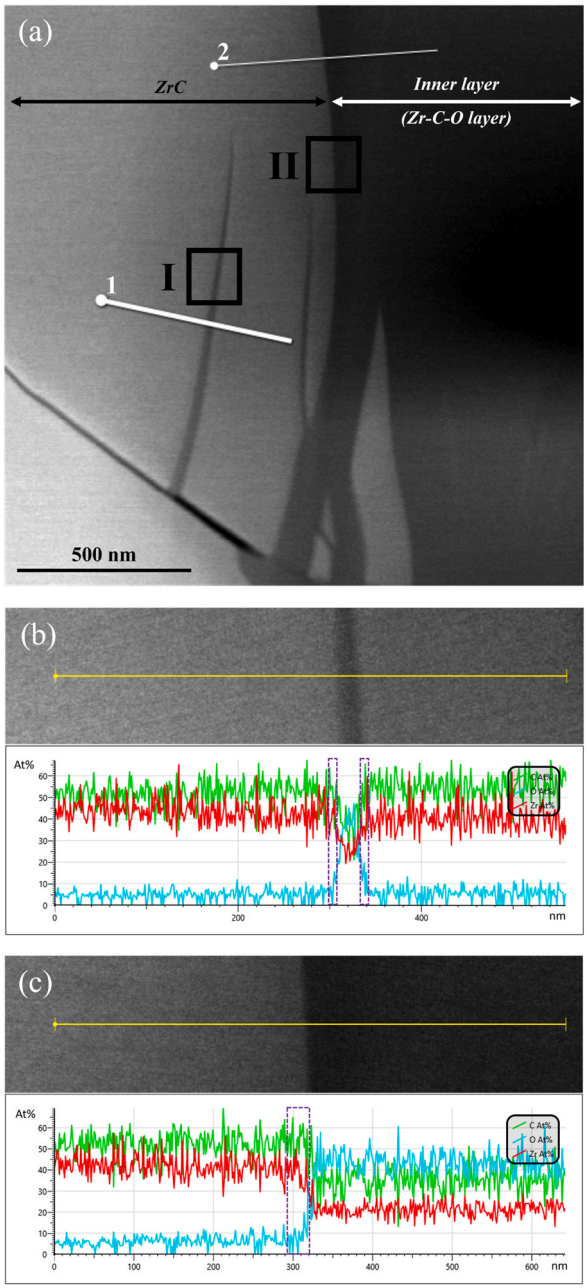

Fig. 2. (a) TEM image at the interface of ZrC substrate and Zr–C–O layer. Line 1 is the HRTEM-EDX line analysis location of (b), and Line 2 is the HRTEM-EDX line analysis location of (c). Square I is the HRTEM image location of the oxidation front stripe (Fig. 3(a)). Square II is the HRTEM image location of the ZrC/Zr–C–O layer interface (Fig. 3(d)). (b) HRTEM-EDX line analysis of Line 1 in (a). (c) HRTEM-EDX line analysis of Line 2 in (a). The purple dashed square regions indicate the onset of the increase in O at% up to the point near its saturation, which reflects the O/Zr atomic percent ratio < 2.

excluded. Raman spectroscopy confirmed t-ZrO_2 at the surface (Fig. 5(c)), while SAEDP (Fig. 1(f)) indicated that the oxidized layer was c-ZrO_2. This suggested that t-ZrO_2 was confined to the near-surface region. Additionally, the D-band (1350 cm^{-1}) and G-band (1580 cm^{-1}) in Fig. 5(c) indicated that free carbon remained. This carbon retention phenomenon is coherent with the findings of Shimada et al. [22] and Bellucci et al. [11].

At 700 °C, the outer-layer oxide scale was composed of c/t-ZrO_2 and m-ZrO_2. Distinct m-ZrO_2 (11−1) crystal plane at $2\theta = 28.10°$ and (111) crystal plane at $2\theta = 31.47°$ were identified after oxidizing for 3000 s, shown in Fig. 6(a), while c/t-ZrO_2 remained as the major composition of the outer-layer oxide scale. The outer-layer oxide scale composition remained stable throughout 3000–10800 s. However, following 32400 s of oxidation, the normalized maximum peak intensities of the m-ZrO_2 (11−1) and (111) planes increased markedly from the values of 0.087 and 0.10 at 10800 s, reaching up to approximately 0.32. Carbon retention was also identified via Raman spectroscopy; however, a significant reduction in carbon content was observed compared to the sample oxidized at 600 °C (Fig. 5(c)). From the Raman spectra of time dependent oxidation at 700 °C (Fig. 6(b)), it was found that free carbon content decreased progressively with increasing oxidation time. After 5400 s, free carbon was nearly completely depleted.

At 800 °C, a substantial amount of m-ZrO_2 was detected via XRD, notably the emergence of (110) crystal plane at $2\theta = 24.42°$. After 1500 s oxidation, the outer-layer oxide scale became a mixed phase of cubic, tetragonal, and monoclinic ZrO_2. When the oxidation duration increased to 10800 s, m-ZrO_2 prevailed as the main composition of the outer-layer oxide scale (Fig. 5(b)). Significant carbon depletion was identified in the outer-layer oxide scale oxidized at 800 °C, which resulted in the near absence of D and G bands of free carbon in the Raman spectrum (Fig. 5(c)).

3.2.2. *Oxide spallation and high-temperature effects*

When temperature increased up to 1000 °C, pronounced scale spallation was observed, leading to the exposure of fresh ZrC surfaces and the consequent appearance of intense ZrC diffraction peaks (Fig. 5(a)(b)). This spallation disrupted the continuity of the outer-layer oxide scale, thereby complicating phase identification. The observed pronounced spallation phenomenon is attributed to grain boundary diffusion and the buildup of internal CO_2 gas pressure under high-temperature oxidation conditions [29].

Prominent D-band and G-band peaks were observed on the surface of ZrC oxidized at 1000 °C (Fig. 5(c)). The intense peaks indicated a considerably greater amount of free carbon compared to lower oxidation temperatures, suggesting that carbon formation occurred more rapidly at 1000 °C—a phenomenon also reported by Gasparrini et al. [8].

In addition to the large amorphous free carbon quantity identified, a high D-band to G-band intensity ratio (I_D/I_G ratio) was identified (Fig. 5(c)). The D-band at 1350 cm^{-1} is commonly known as the disorder or defect band, which becomes active in defective crystallites of graphite, while G-band located at 1580 cm^{-1} is assigned to the C-C stretching vibration (E_{2g}) of graphite which indicates the degree of crystallinity [35,36]. From the Raman spectroscopy results shown for 1000 °C oxidation (Fig. 5(c)), a significantly higher defective graphite was formed on the ZrC surface compared to low temperature oxidation. Under same oxidation duration of 1500 s, I_D/I_G ratio increased to 1.24 at 1000 °C, reflecting enhanced carbon structural disorder and defect density in graphite. The lack of favorable conditions for carbon ordering suggested the rapid formation of amorphous carbon at 1000 °C. In contrast, I_D/I_G ratios were 1.13 at 700 °C and 0.95 at 600 °C, which indicated progressively lower graphite structural disorder with decreasing temperature.

Notably, despite the presence of a G-band in the carbon detected after oxidation, it was broad rather than sharp, which indicated that the graphitic domains were either small in size or structurally disordered. While sp^2 bonding was still present, the lack of long-range order distinguished the detected carbon from well-crystallized graphite.

3.3. *Outer-layer oxide scale growth model*

A phenomenological model was developed to predict the oxide scale growth of SPS-sintered ZrC under different temperatures and oxygen partial pressures. The thickness of the compact Zr–C–O layer was around 3 μm at 600 °C and increased significantly reaching 9–10 μm at 700 °C after oxidation duration of 10800 s. At a fixed temperature, the thickness of the compact Zr–C–O layer showed limited variation across

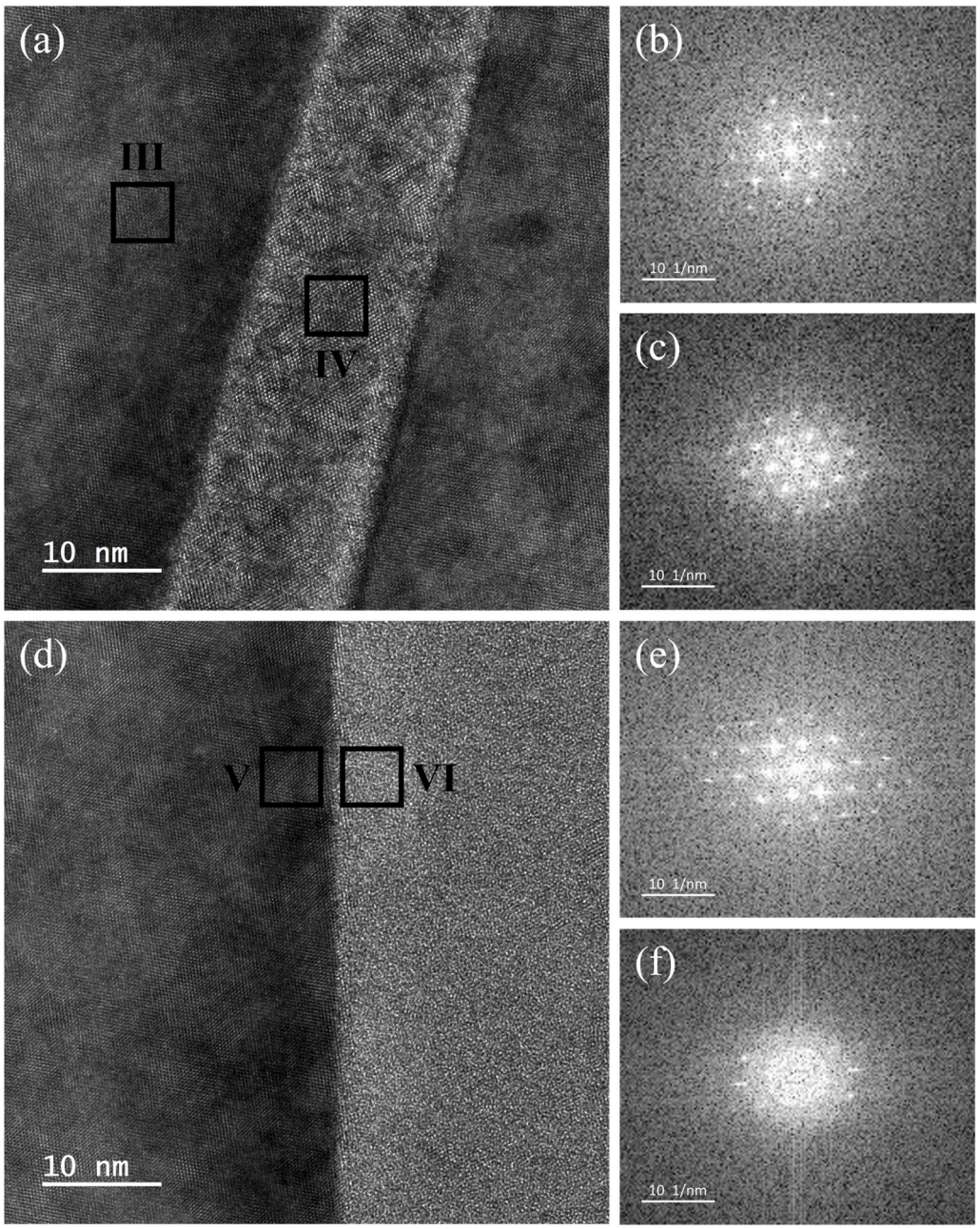

Fig. 3. (a) HRTEM image at the oxidation front stripe with zone axis: [01−1]. The oxidation front stripe is shown in the middle bright region. The location of the HRTEM image is Square I in Fig. 2(a). (b) Cubic FFT pattern of ZrC substrate located at Square III in (a). (c) Cubic FFT pattern of oxidation front strip located at Square IV in (a). (d) HRTEM image at the interface of ZrC (left side) and the Zr–C–O layer (right side) with zone axis: [01−1]. The location of the HRTEM image is Square II in Fig. 2(a). (e) Cubic FFT pattern of ZrC substrate located at Square V in (d). (f) FFT pattern of Zr–C–O layer located at Square VI in (d).

oxygen partial pressures of 2–21 % O_2 after the maximum existence time of the sole compact Zr–C–O monolayer. The sole compact Zr–C–O monolayer reached a thickness of approximately 3.85 ± 0.49 μm at 600 °C and 15.05 ± 0.93 μm at 700 °C prior to the onset of significant CO_2 formation, which led to cracked outer scale and consequently the development of a double-layer oxide scale, as reported by Lin et al. [29].

Shimada [22] reported a zone 1 crack-free layer with constant compact thickness, along with a zone 2 cracked layer that grew linearly with time, resulting in an overall linear oxidation behavior. In a more recent and detailed study, Lin et al. [29] reported the formation of sole compact Zr–C–O monolayer at temperatures approximately and below 700 °C before significant CO_2 formation. Building on previously reported observations [22,29], we proposed a linear dependence of the outer-layer oxide scale thickness on time, and defined a maximum time parameter for the persistence of a sole compact Zr–C–O monolayer before the onset of cracked outer-layer scale formation (t_{max}). Consequently, a linear model incorporating the maximum time parameter (t_{max}) was adopted to characterize the system oxidation behavior, shown in Eq. (7).

$$x = k \cdot (t - t_{max}) \tag{7}$$

where x (μm) is the outer-layer oxide scale thickness, k (μm·s^{-1}) is the outer-layer oxide scale thickness growth rate constant, t (s) is the total oxidation duration, and t_{max} (s) is the maximum existence time of the sole compact Zr–C–O monolayer before forming cracked outer-layer oxide scale. For instance, t_{max} is 4000 at 600 °C, 1500 at 700 °C, and 0 at 800 °C under 2 % O_2 according to the 2D oxidation time-oxygen

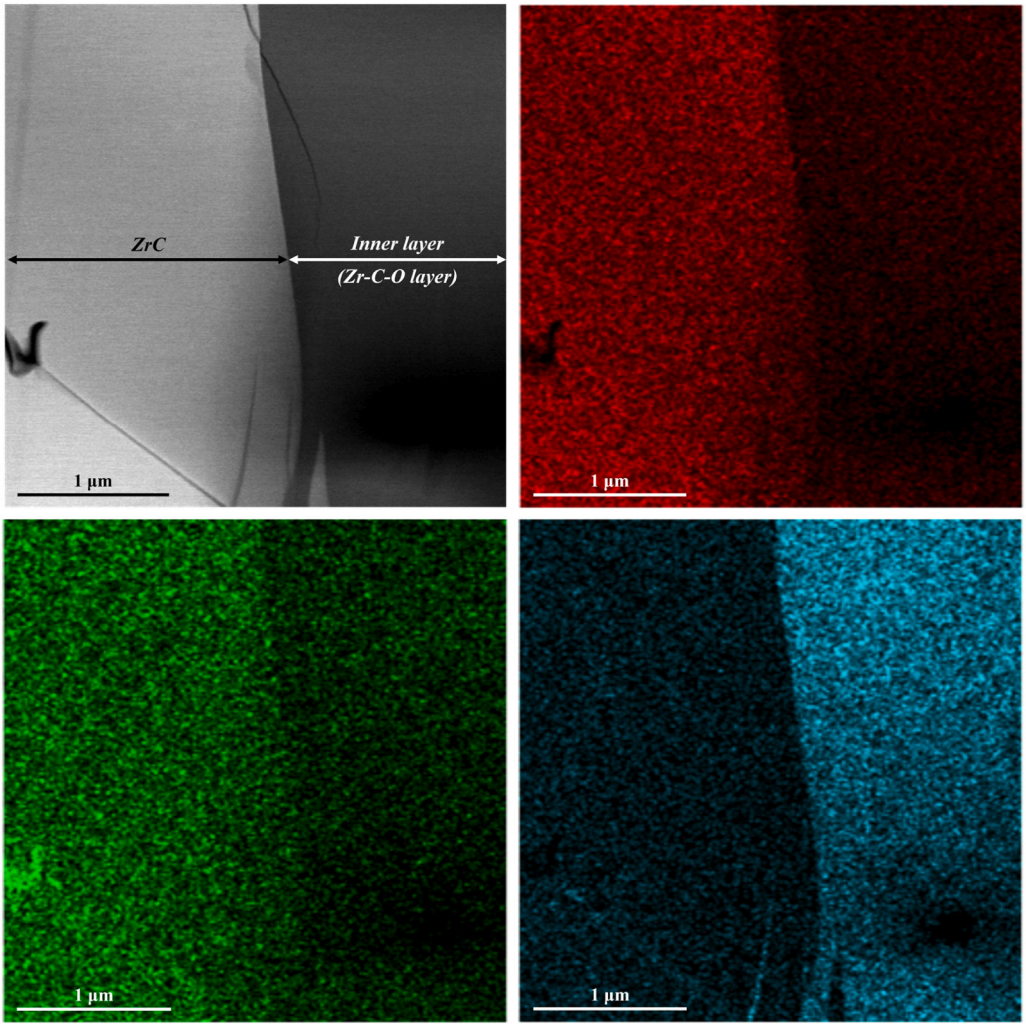

Fig. 4. HRTEM-EDX elemental mapping at the ZrC substrate/Zr–C–O layer interface. Zr distribution is shown in red, C in green, and O in blue.

partial pressure (t-P) projection which delineated the transition boundary of carbon retention and carbon oxidation established by Lin et al. [29]. The t_{max} values under 600–800 °C at 2.0–21.0 % O_2 are shown in Table 3.

We initiated the construction of the phenomenological model using oxygen partial pressure of 2 % O_2. Under this condition, k were determined to be 6.0×10^{-4}, 7.5×10^{-3}, and 2.1×10^{-2} (μm/s) at temperatures of 600 °C, 700 °C, and 800 °C, respectively, based on measurements of the outer-layer oxide scale thickness over the isothermal oxidation duration of 10800 s. From the outer-layer oxide scale thickness growth rate constant (k), activation energy (E_a) was derived using Arrhenius plot in temperature 600–800 °C with a value of 139966 J·mol^{-1}. The outer-layer oxide scale thickness growth rate k is described as Eq. (8).

$$k = A \cdot e^{\left(-\frac{E_a}{RT}\right)} \tag{8}$$

where A (μm·s^{-1}) is the pre-exponential factor, E_a (J·mol^{-1}) is the activation energy derived from the outer-layer oxide scale thickness growth rate constant with a value of 139966, R (J·K^{-1}·mol^{-1}) is the universal gas constant, and T (K) is the oxidation temperature. Next, we introduced pressure dependent pre-exponential factor. k can thus be written as Eq. (9).

$$k = \alpha \cdot P_{O_2}^{m} \cdot e^{\left(-\frac{139966}{RT}\right)} \tag{9}$$

where k (μm·s^{-1}) is the outer-layer oxide scale thickness growth rate constant, α (μm·s^{-1}·(% O_2)$^{-m}$) is the pressure dependent pre-exponential factor, P_{O_2} (% O_2) is the oxygen partial pressure, m is the power related to P_{O_2}, R (J·K^{-1}·mol^{-1}) is the universal gas constant, and T (K) is the oxidation temperature. Substitution of Eq. (9) into Eq. (7) yields Eq. (10):

$$x = \alpha \cdot (t - t_{max}) \cdot e^{\left(-\frac{139966}{RT}\right)} \cdot P_{O_2}^{m} \tag{10}$$

where α and m were determined through power-law fitting of the outer-layer oxide scale thickness (x) as a function of oxygen partial pressure (PO_2). The data are depicted in a log–log plot (Fig. 7), displaying a linear trend that corroborates the applicability of the power-law relationship. The parameter α reflects the intrinsic rate constant modulated by oxygen partial pressure while m captures the sensitivity of the growth rate to oxygen concentration. The values of x in Eq. (10) were measured from SEM images of ZrC samples oxidized isothermally for a duration $t = 10800$ s. t_{max} used for the fitting were 2750 s at 600 °C, 675 s at 700 °C, and 0 s at 800 °C, corresponding to the average t_{max} values observed under the investigated oxygen partial pressure range. The power-law fits exhibited coefficients of determination (R^2) of 0.98,

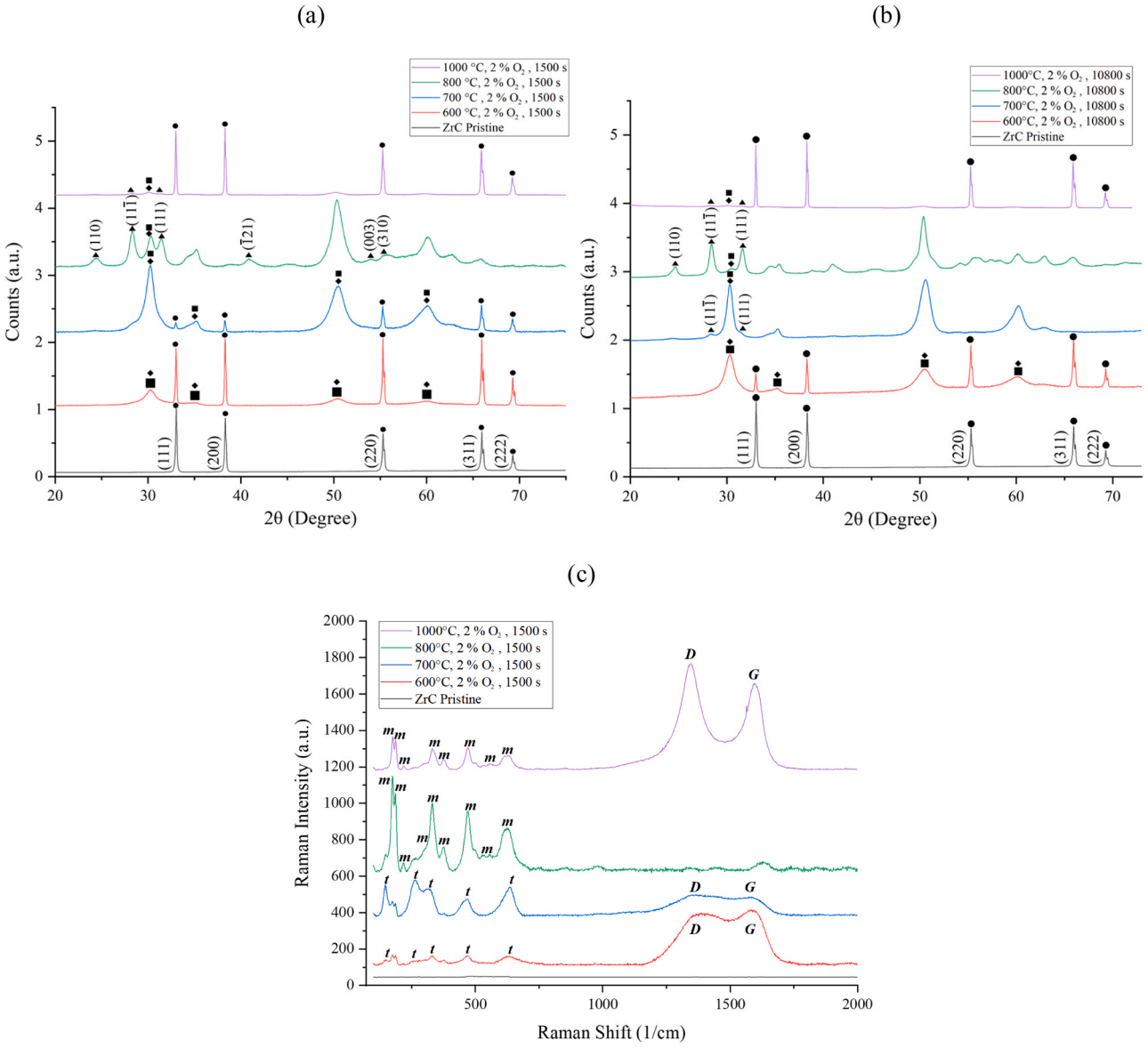

Fig. 5. (a)(b) XRD patterns of temperature dependent oxidation. (a) Oxidation duration: 1500 s. (b) Oxidation duration: 10800 s. ●: ZrC; ■: c-ZrO_2; ◆: t-ZrO_2; ▲: m-ZrO_2. (c) Raman spectra of temperature dependent oxidation. t: t-ZrO_2; m: m-ZrO_2; D: D-band of free carbon; G: G-band of free carbon. t-ZrO_2 Raman peaks: 150, 272, 315, 462, 642 cm^{-1}. m-ZrO_2 Raman peaks: 179, 188, 222, 307, 334, 344, 381, 480, 557, 617, 632 cm^{-1}. Raman peaks of carbon: D-band at 1350 cm^{-1}, and G-band at 1580 cm^{-1}.

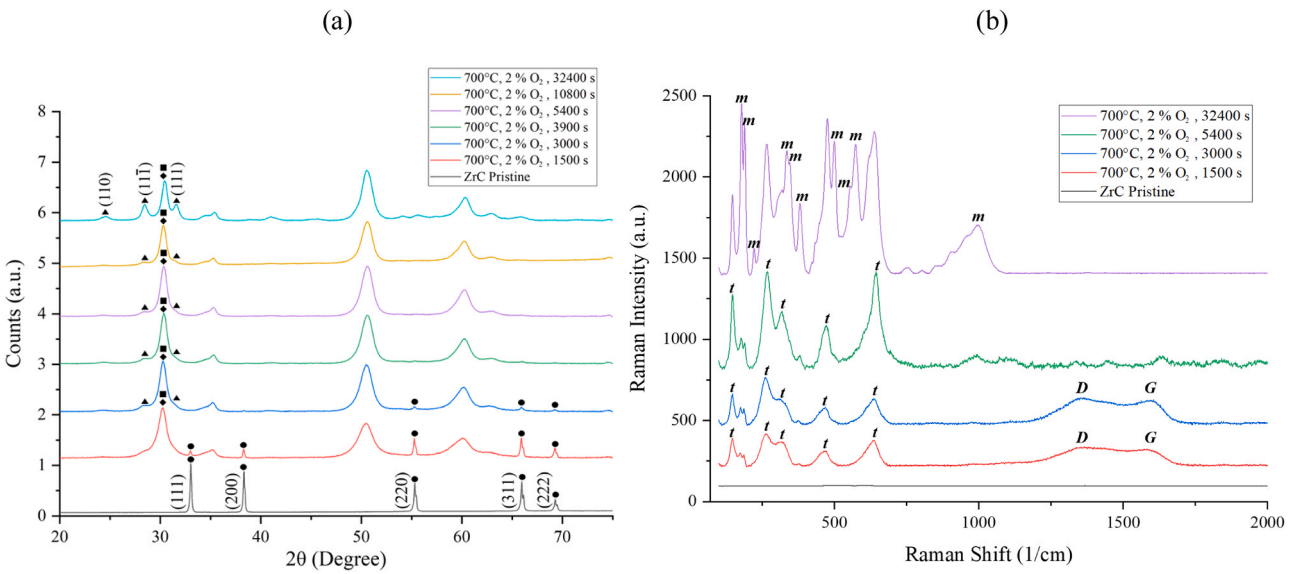

Fig. 6. (a) XRD patterns of time dependent oxidation at 700 °C; 2 % O_2. ●: ZrC; ■: c-ZrO_2; ◆: t-ZrO_2; ▲: m-ZrO_2. (b) Raman spectra of time dependent oxidation at 700 °C; 2 % O_2. t: t-ZrO_2; m: m-ZrO_2; D: D-band; G: G-band of free carbon.

Table 3
t_{max} (s) under 600–800 °C and 2.0–21.0 % O_2.

PO_2 (% O_2) Temp (°C)	2.0	5.0	10.0	21.0
600	4000 s	4000 s	2000 s	1000 s
700	1500 s	500 s	500 s	200 s
800	0 s	0 s	0 s	0 s

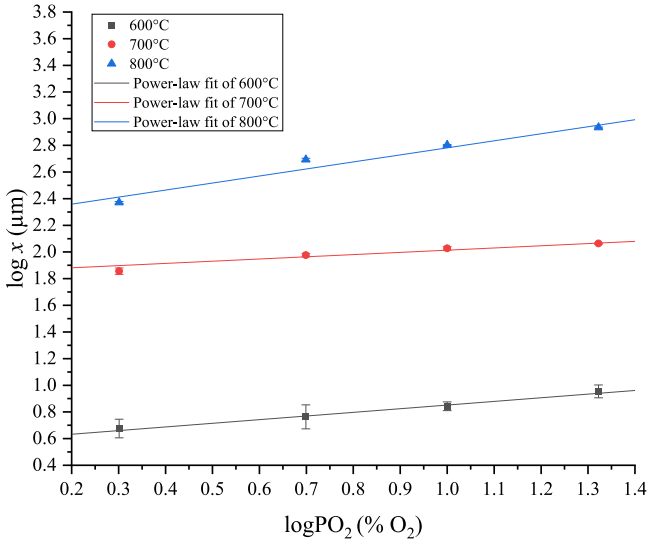

Fig. 7. Log–log plot of outer-layer oxide scale thickness (x) versus oxygen partial pressure (PO_2) at 600 °C (black), 700 °C (red), and 800 °C (blue). Symbols represent experimental data with error bars indicating standard deviations transformed into log space. Solid lines correspond to power-law fits, which appear linear on the log–log scale.

0.97, and 0.97 at 600 °C, 700 °C, and 800 °C, respectively. The resulting power-law fitting parameters, α and m, are presented in Table 4.

The final model, established in the following Eq. (11), captures the dependence of outer-layer oxide scale growth on temperature (T), oxygen partial pressure (P_{O_2}), and time (t). At given temperature and

Table 4
α and m under different temperatures.

Temperature (°C)	α (μm·s^{-1}·(% O_2)$^{-m}$)	m
600	112905	0.27
700	217930	0.19
800	107065	0.54

oxygen partial pressure, the outer-layer oxide scale growth can be predicted as a function of time.

$$x = \alpha \cdot e^{\left(-\frac{139966}{RT}\right)} \cdot P_{O_2}^{m} \cdot (t - t_{max}) \tag{11}$$

However, at temperature exceeding 800 °C, oxide spallation introduced discontinuities in scale growth, violating the assumptions of continuous layer formation. Future models may need to incorporate mechanical failure or gas pressure buildup dynamics.

The model's predictions under 600–800 °C were compared with experimental measurements, as shown in Table 5 and Table 6. The standard deviations were rounded to two significant figures, and the means were reported with matching decimal precision. Model-predicted values were expressed with precision equivalent to the corresponding experimental means to avoid implying greater accuracy. Absolute percentage errors (APE) were calculated from Eq. (12) with the full-precision values, and rounded to one decimal place to provide a clear and consistent assessment of model performance. The model demonstrated satisfactory accuracy, with APE below 20.0 %.

$$APE = \left|\frac{Model\ Predicted\ Value - Mean\ Experimental\ Value}{Mean\ Experimental\ Value}\right| \times 100\ \% \tag{12}$$

To further enhance the predictive fidelity of oxide scale growth under service-relevant conditions, future research could focus on integrating advanced Finite Element Modeling (FEM) approaches with multilayer diffusion frameworks. This would improve the model's ability to simulate the complicated interplay between transport kinetics and mechanical constraints, encompassing oxide scale spallation which may arise from stress accumulation and/or grain boundary diffusion.

Table 5
Comparison between model predictions and experimental values at 10800 s. The model-predicted values are obtained from the established phenomenological oxide scale growth model. The mean experimental values represent the average of repeated experimental measurements, and the standard deviation quantifies the variability in the experimental data.

Temp (°C)	600				700				800			
PO_2 (% O_2)	2.0	5.0	10.0	21.0	2.0	5.0	10.0	21.0	2.0	5.0	10.0	21.0
Model-predicted value (μm)	3.91	5.0	7.83	10.7	70.7	93.1	106.2	125.7	258.3	424	617.7	923.1
Mean experimental value (μm)	4.74	5.8	6.96	9.0	71.8	94.8	106.4	115.9	234.9	492	633.6	858.2
Standard deviation (μm)	0.76	1.2	0.52	1.0	4.0	2.9	3.1	1.5	4.1	12	6.4	8.4
Absolute percentage error (%)	17.5	13.8	12.5	18.9	1.5	1.8	0.2	8.5	10.0	13.8	2.5	7.6

Table 6
Comparison between model predictions and experimental values at 700 °C. The model-predicted values are obtained from the established phenomenological oxide scale growth model. The mean experimental values represent the average of repeated experimental measurements, and the standard deviation quantifies the variability in the experimental data.

PO_2 (% O_2)	2.0			21.0
Time (s)	3000	5400	10800	32400
Model-predicted value (μm)	11.4	29.7	70.7	385.9
Mean experimental value (μm)	12.4	31.4	71.8	388.7
Standard deviation (μm)	1.3	3.9	4.0	4.4
Absolute percentage error (%)	8.1	5.4	1.5	0.7

4. Conclusions

This study presented a comprehensive investigation of oxide growth spanning from nanoscale to macroscale dimensions. HRTEM was employed to analyze the oxidation front stripes and Zr–C–O layer at the nanoscale and microscopic levels providing detailed structural and compositional insights. Furthermore, a robust phenomenological model incorporating temperature, oxygen partial pressure, and dense Zr–C–O layer formation effects was developed to capture the oxide scale thickness growth across mesoscopic and macroscopic regimes. By bridging nanoscale oxidation mechanisms and bulk material performance, the multiscale approach provides a framework for the rational design of ultra-high temperature ceramics. This integrated study highlights the three principal conclusions regarding the mechanism and behavior of oxide growth in spark plasma sintered ZrC:

(1) Oxidation front stripes, Zr–C–O layer, and interfaces

For the first time, the oxidation front stripes of spark plasma sintered ZrC were observed and investigated. The oxidation front stripe and Zr–C–O layer consisted primarily of c-ZrO_2, with the Zr–C–O layer exhibiting significant enrichment of amorphous free carbon. Elliptical pores ranging from the nanometer to submicrometer scale were discovered along the oxidation front stripes, suggesting a preferred pathway for CO_2 release in early-stage oxidation. The oxycarbide phase was not detected in the oxidation front stripes or the Zr–C–O layer. However, a nanoscale transitional zone observed via HRTEM-EDX may correspond to the compositional range in which zirconium oxycarbide could exist.

(2) Outer-layer oxide scale response under elevated temperatures

At 600 °C, the outer-layer oxide scale remained predominantly c-ZrO_2, with t-ZrO_2 present at the outermost surface. Increasing the temperature to 700 °C led to the formation of m-ZrO_2, which became the dominant oxide phase at 800 °C. At 1000 °C, defective graphite was abundant, with a high I_D/I_G ratio and severe oxide spallation. The broad D and G bands indicate a lack of long-range order, distinguishing this carbon from well-crystallized graphite. In addition, the oxycarbide phase was not detected in the outer-layer oxide scale.

(3) Phenomenological oxide scale growth model

The first phenomenological oxide growth model of SPS-sintered ZrC incorporating three effects—temperature, oxygen partial pressure, and compact Zr–C–O layer formation effects—was developed for isothermal oxidation. The model predicts outer oxide scale thickness for 600–800 °C and 2.0–21.0 % O_2 with APE below 20.0 %, providing a reliable tool to optimize ZrC-based materials for aerospace and nuclear applications. However, its applicability is limited to temperatures up to 800 °C due to severe oxide scale spallation. Integrating atomic-scale simulations with spallation dynamics could further extend its predictive capabilities and support the deployment of ZrC ultra-high temperature ceramic in extreme environments.

CRediT authorship contribution statement

Yun-Ching Lin: Writing – review & editing, Writing – original draft, Visualization, Validation, Methodology, Investigation, Formal analysis, Data curation, Conceptualization. **Richard Huizenga:** Validation, Resources, Investigation. **Hyun-Sik Kim:** Validation, Resources, Investigation. **Hans Brouwer:** Validation, Resources, Investigation. **Amir Mohseni Armaki:** Validation, Investigation. **Vera Popovich:** Writing – review & editing, Supervision, Resources. **Yinglu Tang:** Writing – review & editing, Validation, Supervision, Methodology, Funding acquisition, Conceptualization.

Declaration of Competing Interest

The authors declare that they have no known competing financial interests or personal relationships that could have appeared to influence the work reported in this paper

Acknowledgements

The authors acknowledge Junsu Kim (Department of Materials Science and Engineering, University of Seoul) for assistance with HRTEM analysis.

References

[1] G.R. Peterson, R.E. Carr, E.E. Marinero, Zirconium carbide for hypersonic applications, opportunities and challenges (art. no), Materials 16 (2023) 6158.
[2] A. Savvatimskiy, Experimental study of high-temperature properties of zirconium carbide as a protective material for nuclear power and aerospace technologies (from 2000 to 5000 K), J. Phys. Conf. Ser. 891 (1) (2017) 012318.
[3] H.O. Pierson, Handbook of refractory carbides and nitrides: properties, characteristics, processing and applications, Noyes Publications, 1996.
[4] W.G. Fahrenholtz, E.J. Wuchina, W.E. Lee, Y. Zhou, Ultra-high temperature ceramics: materials for extreme environment applications, John Wiley & Sons, 2014.
[5] M. Sheindlin, T. Falyakhov, S. Petukhov, G. Valyano, A. Vasin, Recent advances in the study of high-temperature behaviour of non-stoichiometric TaC_x, HfC_x and ZrC_x carbides in the domain of their congruent melting point, Adv. Appl. Ceram. 117 (S1) (2018) S48–S55.
[6] R.F. Voitovich, E.A. Pugach, High-temperature oxidation of ZrC and HfC, Sov. Powder Metall. Met. Ceram. 12 (1973) 916.
[7] Z. Huang, Z. Zhu, M. Su, Y. Shi, M. Deng, R. Chen, Z. Wang, Z. Zhou, J. Qi, H. Wang, High-temperature oxidation behaviors of dense TMC (TM= Ta, Nb, Ti, and Zr) ceramics in air (part A), Ceram. Int. 49 (23) (2023) 38036–38046.
[8] C. Gasparrini, R.J. Chater, D. Horlait, L. Vandeperre, W.E. Lee, Zirconium carbide oxidation: kinetics and oxygen diffusion through the intermediate layer, J. Am. Ceram. Soc. 101 (2018) 2638–2652.
[9] C. Gasparrini, R. Podor, D. Horlait, R. Chater, W.E. Lee, Zirconium carbide oxidation: maltese cross formation and interface characterization, Oxid. Met. 88 (2017) 509–519.
[10] S. Shimada, M. Inagaki, M. Suzuki, Microstructural observation of the ZrC/ZrO_2 interface formed by oxidation of ZrC, J. Mater. Res. 11 (1996) 2594–2597.

[11] A. Bellucci, D. Gozzi, T. Kimura, T. Noda, S. Otani, Zirconia growth on zirconium carbide single crystals by oxidation, Surf. Coat. Technol. 197 (2005) 294–302.
[12] S. Shimada, M. Nishisako, M. Inagaki, K. Yamamoto, Formation and microstructure of carbon-containing oxide scales by oxidation of single crystals of zirconium carbide, J. Am. Ceram. Soc. 78 (1) (1995) 41–48.
[13] Z. Ye, Y. Zeng, X. Xiong, T. Qian, H. Lun, Y. Wang, W. Sun, Z. Chen, New insight into the formation and oxygen barrier mechanism of carbonaceous oxide interlayer in a multicomponent carbide, J. Am. Ceram. Soc. 103 (2020) 6978–6990.
[14] Y. Katoh, G. Vasudevamurthy, T. Nozawa, L.L. Snead, Properties of zirconium carbide for nuclear fuel applications, J. Nucl. Mater. 441 (2013) 718–742.
[15] R.W. Bartlett, M.E. Wadsworth, I.B. Cutler, The oxidation kinetics of zirconium carbide, Trans. AIME 227 (1963) 467–472.
[16] G.A. Rama Rao, V. Venugopal, Kinetics and mechanism of the oxidation of ZrC, J. Alloy. Compd. 206 (1994) 237–242.
[17] S. Shimada, M. Nishisako, M. Inagaki, Formation and microstructure of carbon-containing oxide scales by oxidation of single crystals of zirconium carbide, J. Am. Ceram. Soc. 78 (1) (1995) 41–48.
[18] S. Shimada, T. Ishii, Oxidation kinetics of zirconium carbide at relatively low temperatures, J. Am. Ceram. Soc. 73 (10) (1990) 2804–2808.
[19] S. Shimada, Microstructural observation of ZrO_2 scales formed by oxidation of ZrC single crystals with formation of carbon, Solid State Ion. 101–103 (1997) 749–753.
[20] S. Shimada, TEM observation of the ZrC/ZrO_2 interface formed by oxidation of ZrC single crystals, J. Mater. Synth. Process 6 (3) (1998).
[21] S. Shimada, M. Yoshimatsu, M. Inagaki, S. Otani, Formation and characterization of carbon at the ZrC/ZrO_2 interface by oxidation of ZrC single crystals, Carbon 36 (7–8) (1998) 1125–1131.
[22] S. Shimada, Interfacial reaction on oxidation of carbides with formation of carbon, Solid State Ion. . 141–142 (2001) 99–104.
[23] S. Shimada, Oxidation and mechanism of single crystal carbides with formation of carbon, J. Ceram. Soc. Jpn. 109 (3) (2001) S33–S42.
[24] S. Kwon, A. Rajkamal, J. An, G.J. Yun, Mechanisms of oxycarbide formation on ZrC, HfC, and TaC surfaces during early oxidation: insights from computational simulations, Ceram. Int. 51 (2025) 14755–14766.
[25] X.-M. Hou, K.-C. Chou, Investigation of the effects of temperature and oxygen partial pressure on oxidation of zirconium carbide using different kinetics models, J. Alloy. Compd. 509 (2011) 2395–2400.
[26] K.-C. Chou, X.-M. Hou, Kinetics of high-temperature oxidation of inorganic nonmetallic materials, J. Am. Ceram. Soc. 92 (2009) 585–594.
[27] K.-C. Chou, A kinetic model for oxidation of Si–Al–O–N materials, J. Am. Ceram. Soc. 89 (2006) 1568–1576.
[28] A.K. Kuriakose, J.L. Margrave, The oxidation kinetics of zirconium diboride and zirconium carbide at high temperatures, J. Electrochem. Soc. 111 (1964) 827.
[29] Y.-C. Lin, H. Brouwer, V. Popovich, Y. Tang, Three-stage oxidation kinetics and passivation mechanism of spark plasma sintered ZrC ultra-high temperature ceramic, J. Eur. Ceram. Soc. 46 (2026) 117757.
[30] E. Osei-Agyemang, J.-F. Paul, R. Lucas, S. Foucaud, S. Cristol, A.-S. Mamede, N. Nuns, A. Addad, Structure and energetics of ZrC(100)||c-ZrO_2(001) interface: a combination of experiments, finite temperature molecular dynamics, periodic DFT and atomistic thermodynamic modeling, Ceram. Int. 48 (15) (2022) 21327–21343.
[31] F. Viñes, C. Sousa, F. Illas, P. Liu, J.A. Rodriguez, Density functional study of the adsorption of atomic oxygen on the (001) surface of early transition-metal carbides, J. Phys. Chem. C. 111 (2007) 1307–1314.
[32] J.A. Rodriguez, P. Liu, J. Gomes, K. Nakamura, F. Viñes, C. Sousa, F. Illas, Interaction of oxygen with ZrC(001) and VC(001): Photoemission and first-principles studies, Phys. Rev. B 72 (2005) 075427.
[33] A. Vojvodic, C. Ruberto, B.I. Lundqvist, Atomic and molecular adsorption on transition-metal carbide (111) surfaces from density-functional theory: a trend study of surface electronic factors, J. Phys. Condens. Matter 22 (2010) 375504.
[34] E. Osei-Agyemang, J.-F. Paul, R. Lucas, S. Foucaud, S. Cristol, A.-S. Mamede, N. Nuns, A. Addad, Characterizing the ZrC(111)/c-ZrO_2(111) hetero-ceramic interface: first principles DFT and atomistic thermodynamic modeling, Molecules 27 (2022) 2954.
[35] M.J. Matthews, M.A. Pimenta, Origin of dispersive effects of the Raman D band in carbon materials, Phys. Rev. B 59 (10) (1999) R6585.
[36] A. Cuesta, P. Dhamelincourt, J. Laureyns, A. Martínez-Alonso, Raman microprobe studies on carbon materials, Carbon 32 (8) (1994) 1523–1532.